Journal of Statistical Physics, Vol. 121, Nos. 5/6, December 2005 (© 2005)
DOI: 10.1007/s10955-005-8664-8

Statistics of Stretching Fields in Experimental Fluid Flows Exhibiting Chaotic Advection

P. E. Arratia[1] **and J. P. Gollub**[1,2]

Received March 14, 2005; accepted June 10, 2005

Stretching fields and their statistical properties are studied experimentally for four distinct two-dimensional time-periodic confined fluid flows exhibiting chaotic advection: a random vortex array for two different Reynolds numbers, a set of parallel shear layers, and a vortex lattice. The flows are driven electromagnetically, and they are studied by means of precise particle velocimetry. We find that for a given flow, the probability distributions of log S (where S is the local stretching in N cycles) can be nearly superimposed for different N when log S is rescaled using the geometrical mean of the stretching distribution. The rescaled stretching fields for a given flow at various N are highly correlated spatially when N is large. Finally, the scaled distributions for *different* flows are similar, though there are some differences connected to the degree of spatial symmetry and time-reversibility of the flows.

KEY WORDS: Stretching statistics; chaotic advection; mixing in fluids.

1. INTRODUCTION

Fluid mixing is an important phenomenon in fundamental statistical mechanics, and also occurs in diverse natural situations. Examples include atmospheric mixing, which influences environmental chemistry and weather,[(1)] and convective mixing within the lungs, which is responsible for gas transport to alveolar surfaces.[(2)] The first step in mixing (or homogenization of a passive impurity) is the stretching of fluid elements into elongated striations. This fact was recognized by Batchelor,[(3)] who first demonstrated qualitatively that material lines and surfaces are stretched exponentially in homogeneous, isotropic turbulent flows. However, exponential

[1]Physics Department, Haverford College, Haverford, PA 19041, USA.
[2]Physics Department, University of Pennsylvania, Philadelphia, PA 19104, USA; e-mail: jgollub@haverford.edu

stretching of material elements also occurs in flows exhibiting "chaotic advection",[4] in which even time-periodic two-dimensional velocity fields can create complex distributions of an advected field. In this paper, we measure the statistical properties the stretching fields produced by such time-periodic flows.

One of the key properties of flows exhibiting chaotic advection is the exponential divergence of nearby trajectories in real space, usually characterized by the largest local finite time Lyapunov exponent λ over a time interval Δt (measured in periods). If one imagines the deformation of an infinitesimal circular fluid element located initially at (x, y), the stretching S is defined as the ratio of the final major diameter (after Δt) to the initial diameter. Then $\lambda = (\log S)/\Delta t$. Stretching in these flows is far from uniform;[5–7] it is typically a strong function of space. We refer to this spatially varying function as a "stretching field" $S(x, y)$. For time-periodic flows, the stretching field is also a function of phase, but it is typically sufficient to focus attention on a single phase. The statistical properties of $S(x, y)$ or $\lambda(x, y)$ strongly affect fluid mixing rates,[8,9] and the fractal properties of scalar gradients.[10,11]

Several aspects of the probability distributions of S or λ have been explored *numerically* in chaotic flows. For example, Ottino *et al.*[5] showed that the stretching distributions $H_N(\log S)$ for various numbers N of cycles exhibit self-similar behavior; the distributions for all N can be superimposed when S is plotted as a rescaled variable $z = (\log S)/(\log S_g)$, where S_g is the geometrical mean stretching (see Eq. 1). This self-similar behavior is found numerically in different types of 2D chaotic flows, ranging from flows that are chaotic everywhere, to others whose Poincaré maps show regular elliptic islands.[12] The distributions converge to different asymptotic forms for flows with and without islands.[13] Self-similarity of stretching distributions is also reported for other types of flows exhibiting chaotic behavior, including models of atmospheric and ocean flows,[14,15] and certain chaotic maps.[6,16] In addition, other results indicate that the first moment of the rescaled distribution converges with increasing time[12,17] and that the variance of the distribution grows as a linear function of time (or N), although an intermediate power-law scaling may occur.[18] Authors differ on the distribution function characterizing stretching values. Some investigations show that the asymptotic distribution can be Gaussian[5,6] for fully chaotic flows while other earlier works[10,11] demonstrate that the distribution of Lyapunov exponents is not necessarily Gaussian. Other aspects of the stretching distributions have also been studied, such as the properties of the high-stretch tail[19] that are often encountered in fully chaotic flows, and the multifractal characteristics that are sometimes noted.[20]

Most investigations of stretching statistics have been restricted to numerical simulations, because of the difficulty of measuring stretching fields in experimental flows. Recently, however, Voth *et al.*[7] demonstrated that it is possible to obtain accurate stretching fields from high spatial resolution velocity fields in time-periodic flows. Therefore, it is now possible to consider the statistical properties of stretching distributions experimentally.

In this paper, we determine the statistics of stretching for four quite different 2D time-periodic velocity fields that exhibit chaotic mixing, using the methods reported by Voth *et al.*[7] All of the flows are created by magnetohydrodynamic forcing of a conducting fluid. The velocity fields have different degrees of symmetry, and regular (non-mixing) regions occur to a different extent in the various flows. We examine the scaling properties of the stretching distributions of these flows, and compare the distributions with each other.

2. EXPERIMENTS

We investigate mixing in an electromagnetically driven fluid layer (Fig. 1) as explained in ref. 9. A time-periodic current travels horizontally through a conducting fluid layer that is placed above an array of permanent magnets. The resulting Lorenz forces drive a time-periodic vortex flow that may be spatially ordered or disordered depending on the arrangement of the forcing magnets. The area of fluid flow is 15×15 cm, and all figures in this paper show a central 10×10 cm region. The forcing frequencies used in this investigation are 100 mHz and 68 mHz, and typical velocities are 0.01–0.7 cm/s. The fluids used in this investigation are a

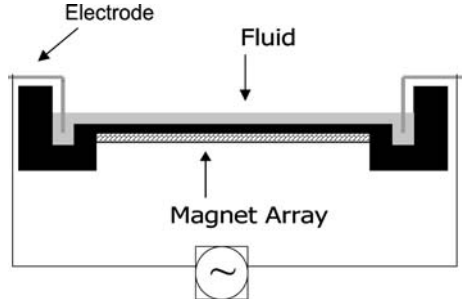

Fig. 1. Schematic diagram of the apparatus for producing two-dimensional, time-periodic flows by passing an AC current through a conductive fluid in the presence of a structured magnetic field. The fluid is comprised of two layers as indicated in the text.

20% and a 50% aqueous solution of glycerol. The 20% glycerol solution has a fluid viscosity η of 1.74 cP and a fluid density ρ of 1.1 g/cm^3 and it is used for the higher Reynolds number experiments. The 50% solution ($\eta = 6.67$ cP, $\rho = 1.15$ g/cm^3) is used for the low Re flow. The fluids are made conductive by adding KCl salt, 5% by weight. Experiments are performed using two fluid layers. The bottom layer is denser and conductive, and it is about 3 mm in thickness. The upper layer is not conductive (no salt added) and it is 1 mm thick. The flow is essentially two-dimensional.

Particle tracking experiments are performed by seeding the fluid with fluorescent polystyrene spheres 120 μm in diameter. The fluorescent particles are placed at the interface of the two fluid layers. Usually, 600–800 particles are imaged in a single frame. We record up to 8000 images using a CCD camera (512×512) at 8 Hz in a typical run, or 80–100 images per period. The centroid of each particle is found with a precision of 40 μm. Particles found in sequential images are then labeled and combined into tracks. These tracks are then used to obtain velocity fields and to construct Poincaré maps. Because the flow is periodic, we can combine particle positions obtained at a given phase (relative to the forcing) to obtain up to 80,000 precise particle positions at each phase and thereby obtain very high spatial resolution (0.004 of the field of view), excellent time resolution (0.01 and 0.007 of a flow period for the 100 mHz and the 68 mHz cases, respectively) and velocities accurate to a few percent.

The process of extracting stretching fields begins by using polynomial fitting to determine particle velocities, which are then interpolated onto a grid. To measure stretching, we determine the flow map $\vec{x}' = \vec{\Phi}(\vec{x}, t_0, \Delta_t)$, which is a function that specifies the destination vector $\vec{x}'$ at time $t_0 + \Delta_t$ of any fluid particle starting from $\vec{x}$ at time t_0. Flow maps are constructed by integrating hypothetical particle trajectories numerically using the velocity grids. These maps determine the final positions of particles as a function of their initial positions. Because the flow is periodic, $\vec{\Phi}$ becomes the Poincaré map of the flow when Δt equal to one period. The stretching S experienced by a fluid element is determined by the gradients of the flow map. More precisely, it is defined as the square root of the largest eigenvalue of the right Cauchy–Green strain tensor, C_{ij}, at the location of interest: $C_{ij} = (\partial \Phi_k / \partial x_i)(\partial \Phi_k / \partial x_j)$, where the summation is implied over the repeated index $k = 1, 2$. It would also be possible to determine stretching from particle trajectory data. However, it is less accurate[7] than the method presented here.

Two different quantities are computed at each point, which we call future and past stretching. Future stretching is the stretching experienced by a fluid element in the next Δt. Past stretching is the stretching that a fluid element experienced in the previous Δt. These quantities, past and

future stretching, tend to be large on the unstable and stable manifolds of the hyperbolic fixed points of the Poincaré map, respectively. Further detail on the velocimetry measurements and stretching calculations may be found elsewhere.[7]

There are two independent dimensionless parameters for our flows. The Reynolds number, $Re = \rho U L/\eta$, is based on the mean magnet spacing $L = 2\,\text{cm}$, RMS velocity U, fluid density ρ, and fluid viscosity η. The path length, $p = U/Lf$, where f is the driving frequency of the flow, describes the mean displacement of a typical fluid element in one forcing period $(1/f)$ normalized by L. In this paper, we investigate flows with different dynamical features, and different degrees of spatial symmetry and time-reversibility. Flows with spatial and temporal symmetry are known to possess non-mixing regions.[21] Spatial symmetry is explored by using different magnetic arrays: a random array of magnets, which produces a flow with no symmetry; a square lattice magnet array that produces a flow with reflection and discrete translation symmetry along the coordinate axes; and a hexagonal lattice magnet array that produces a set of parallel shear layers. The role of time reversibility on the statistics of stretching is explored by using a flow with little spatial symmetry (random array case) investigated both at $Re = 65$ $(p = 2.5)$ and at $Re = 4.5$ $(p = 1.0)$. The velocity field of the $Re = 4.5$ case departs less from time-reversibility than does the $Re = 65$ case,[9] and therefore shows significant non-mixing regions (regular islands).

3. EXPERIMENTAL RESULTS

3.1. Velocity Fields and Stretching Fields

The various flow patterns investigated in this work are shown in Fig. 2 by means of particle pathlines lasting 4 s. The vortex flows produced by random magnet arrays are shown in (a) and (b). The first case $(Re = 65,\ \ p = 2.5)$ is for an elevated Reynolds number and large path length per cycle, while the second is for a more weakly chaotic case $(Re = 4.5,\ \ p = 1.0)$. In (a), the chaotic sea includes most of the spatial domain, whereas in (b), there are significant non-mixing regions as a result of smaller departures from time-reversibility of the velocity field. However, these regular regions are not visible in the pathline patterns, because the elapsed time is too short.

In Fig. 2(c) we see an ordered vortex pattern produced by a square lattice magnet array. We examine this case because the high spatial symmetry tends to inhibit mixing, as shown in previous work of Voth *et al.*[9]

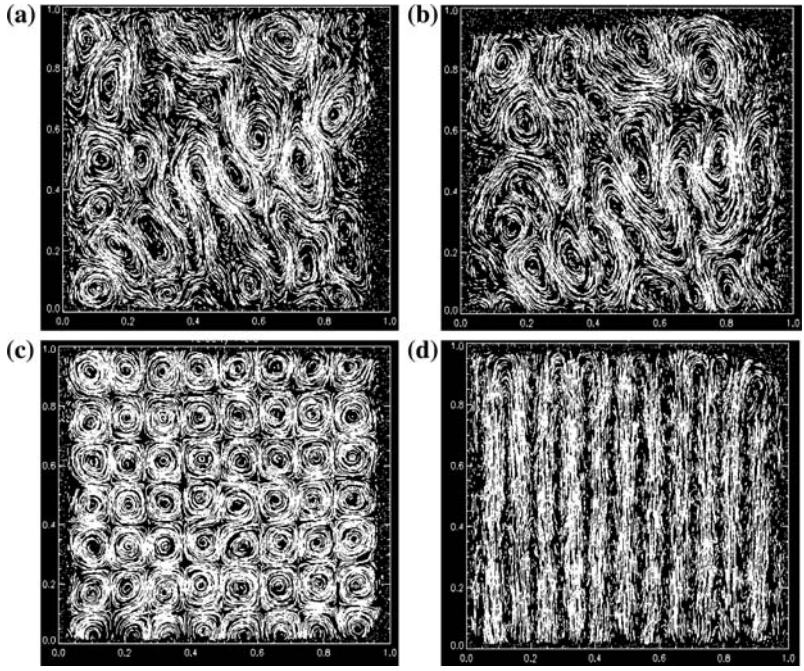

Fig. 2. Path-lines lasting 4 s for (a) a strongly chaotic flow produced by a random magnet array ($Re = 65,\ p = 2.5$); (b) a weakly chaotic flow with non-mixing regions, produced the same array at lower Re ($Re = 4.5,\ p = 1.0$); (c) an ordered vortex pattern produced by a square lattice magnet array ($Re = 65,\ p = 2.5$); and (d) multiple shear layers ($Re = 65,\ p = 2.5$) produced by a hexagonal lattice magnet array.

Finally, Fig. 2(d) shows a parallel shear flow with multiple shear layers produced by a hexagonal lattice magnet array. In (c) and (d) precisely half the magnets have their north poles pointing vertically upward. The measured instantaneous velocity fields in these four cases are given in Fig. 3. These flows are representative of the various flow patterns that can be achieved in a closed (bounded) two-dimensional domain.

Chaotic mixing for these flows depends on the relatively small lack of time-reversibility that occurs as a result of the finite value of Re. This property is evident by looking at Poincaré maps, as shown in Fig. 4. The particle displacements are generally largest for the high Re "random" vortex flow, as a consequence of both the large Re and the lack of symmetry. In (b) there are significant empty regions, which are probably non-mixing regions around elliptic fixed points of the Poincaré maps. Particles inside these regions cannot leave, and particles outside cannot enter them. In

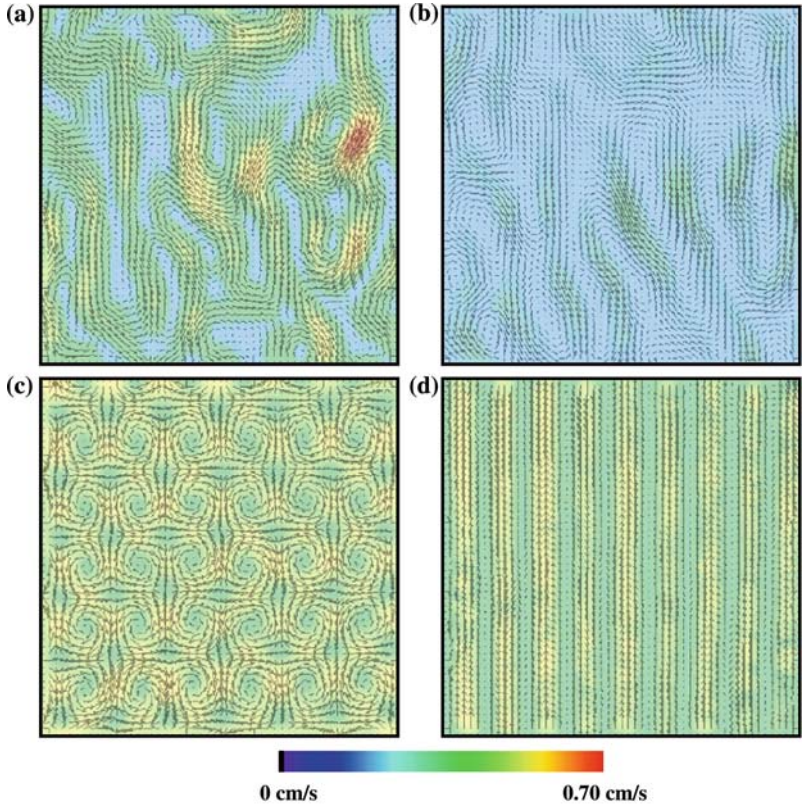

Fig. 3. (Color online) Instantaneous velocity fields for the four flows shown in Fig. 2. Both color coding and arrow lengths are used to show the magnitude and direction of the velocity.

(c) the regions of large displacement are localized around the stagnation (hyperbolic) points of the ordered array of vortices. Finally, in (d) it is interesting to note that the largest displacements after a full cycle are not strictly parallel to the local shear velocity. We do not know why this is the case, but it could be due to large scale convective motion.

Future and past stretching fields for the four flows are shown in Fig. 5. They are quite different from each other. The strongest stretching occurs for (a), as expected from the large particle displacements or large departure from time reversibility of this flow. The stretching field is weak in (b) as a result of the near time-reversibility of the velocity field, even though the spatial structure is similar to that in (a). In the regular array (c), it is particularly clear that the stretching is highly inhomogeneous, being much larger along lines passing through stagnation

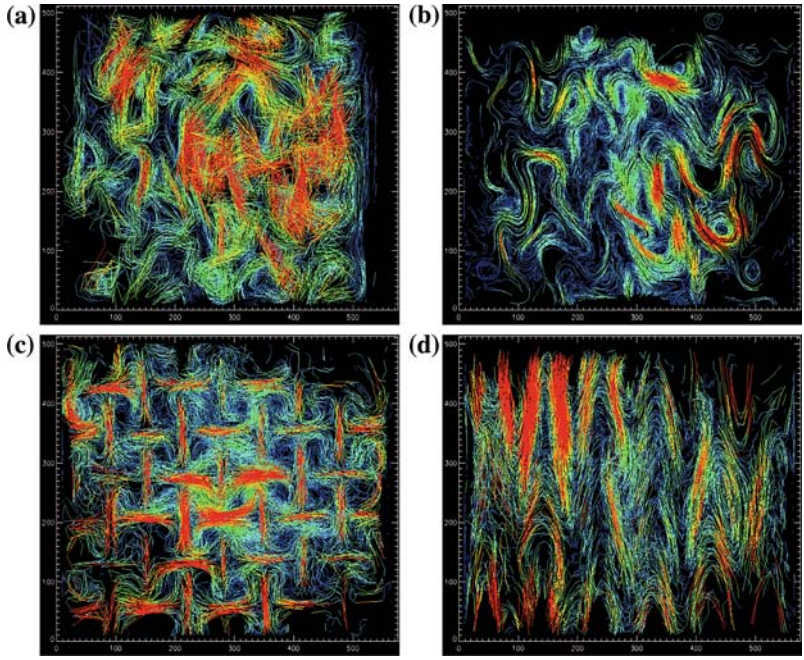

Fig. 4. (Color online) Poincaré Maps of the flows shown in Fig. 2. Lines are drawn between the initial and final positions of particles one period apart. Color is also used online, with red indicating the largest displacements scaled by the maximum displacement (ξ) of each flow. (a) Random array ($Re = 65$, $p = 2.5$, $\xi = 1.2$ cm); (b) random array ($Re = 4.5$, $p = 1.0$, $\xi = 0.48$ cm); (c) regular array ($Re = 65$, $p = 2.5$, $\xi = 0.75$ cm); and shear layer ($Re = 65$, $p = 2.5$, $\xi = 0.75$ cm).

(hyperbolic) points of the flow than in other regions, by a factor of 1000 or more. The stretching field is (d) is highly inhomogeneous but devoid of lines of high stretching as in (c) since there are few hyperbolic points in the flow.

3.2. Statistics of the Stretching Fields

As explained in Section 1, previous analysis and numerical work suggests that stretching fields should have similar structure for different numbers of periods. We test this expectation qualitatively in Fig. 6 for the low *Re* random array of Fig. 2(b) or 3(b). We note that stretching field possesses strong spatial heterogeneity. However, except for the magnitude of stretching values, which increases with N, the fields are similar. (We quantify this statement in the following discussion.)

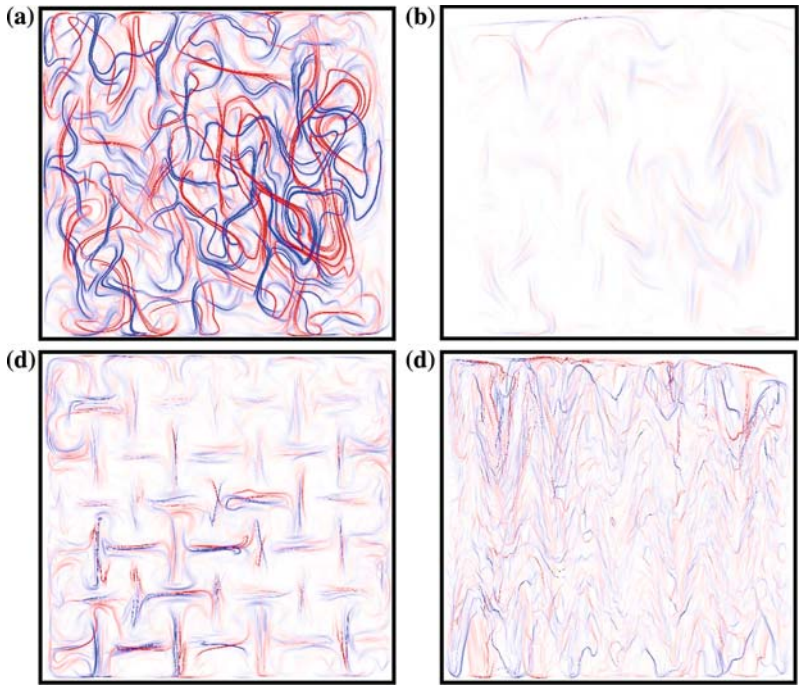

Fig. 5. (Color online) Lines of future and past stretching fields for the four flows of Fig. 2 computed over one period of the dynamics. In the color version, red is used for future stretching, and blue is used for past stretching. The four flows produce quite different stretching fields. The dynamical range of these measurements is at least 5 orders of magnitude.

The statistical distributions of the stretching are shown in Fig. 7. Because the logarithm of the stretching is proportional to the distribution of finite time Lyapunov exponents, we actually plot the probability density function (PDF) of $\log S$, rather than the PDF of S itself. The PDF of $\log S$ is defined as $H(\log S) = \mathrm{d}n(\log S)/\mathrm{d}(\log S)$, where $\mathrm{d}n(\log S)$ is the number of points with values of $\log S$ between $\log S$ and $\log S + \mathrm{d}(\log S)$. It may be seen that for all of the flows, the distributions are peaked, and they become wider as the number of cycles N over which they are computed increases. The mode of the distribution also increases with N.

Next, we explore the scaling properties of these distributions by rescaling the logarithm of the stretching values by the logarithm of the geometrical mean of the stretching (S_g). The logarithm of the geometric mean stretching is equivalent to the arithmetic mean of $\log S$

$$\log S_g = \frac{\int (\log S) H(\log S) \mathrm{d} \log S}{\int H(\log S) \mathrm{d} \log S}. \tag{1}$$

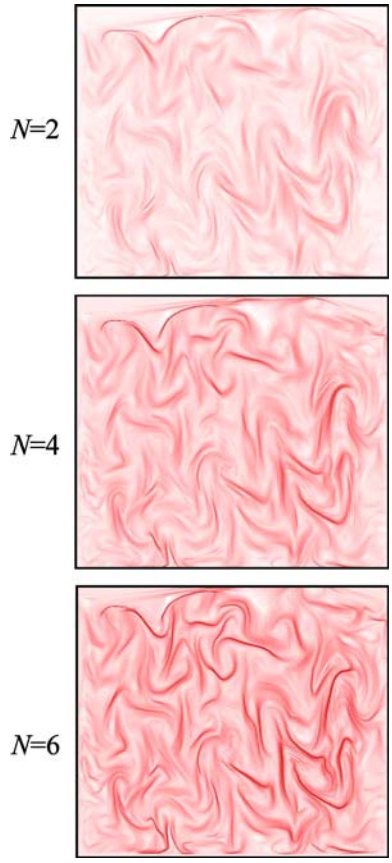

Fig. 6. (Color online) Evolution of the future stretching field as a function of the number of periods N over which it is computed, for the low Re random array of Fig. 2(b) or 3(b). Except for the magnitude of stretching, which increases with N, the fields are similar.

The results for the distribution of the rescaled stretching values are displayed in Fig. 8., where we introduce a variable $z = (\log S)/(\log S_g)$. This quantity z is equivalent to $(\log S)/(\langle\lambda\rangle \Delta t)$, where $\langle\lambda\rangle$ is the average finite time Lyapunov exponent. It may be seen that there is a substantial degree of collapse of the distributions for each of the flows, although it is not perfect. In Fig. 8(b), the rescaled stretching distributions are nearly identical for large N, as one might expect. For the other cases (Fig. 8a–d), the collapse is not as complete. Note that the frequency of occurrence of $S = 1$ or $\log S = 0$ (i.e. no stretching) is non-zero; this indicates that some regions of these flows are not chaotic, at least for flows (b, c, and d). We find that the

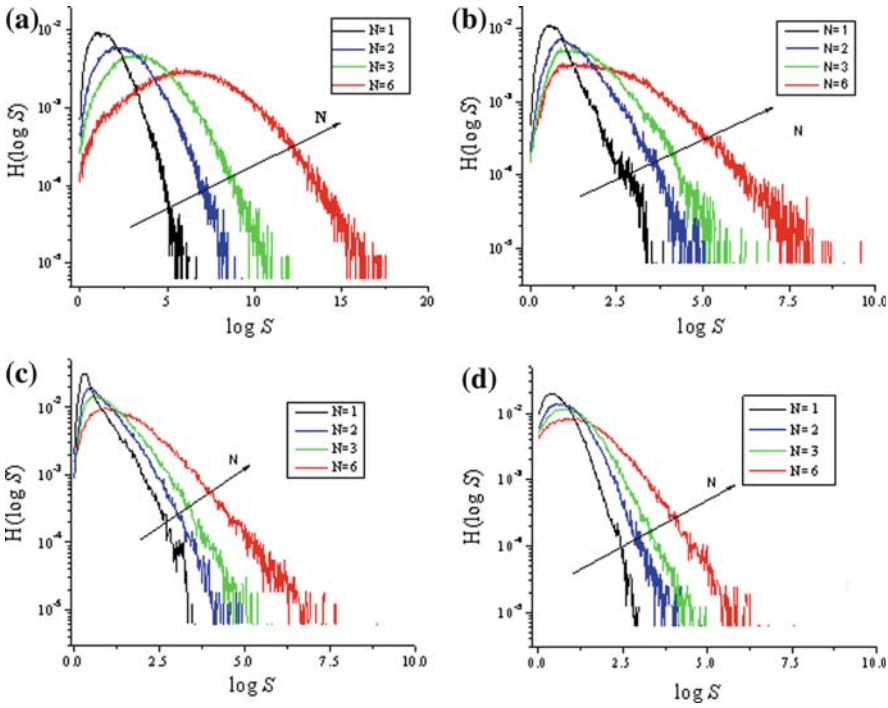

Fig. 7. (Color online) Probability density function of the logarithm of the future stretching S, computed over various numbers of cycles N, for each of the flows of Figs. 2 and 3: $N = 1$ (black), 2 (blue), 3 (green), and 6 (red). All of the distributions have similar peaked shapes and become wider for large N.

distributions are *not* lognormal. There are enhanced tails on the high end part of the rescaled stretching distribution for all flows, rendering the distributions asymmetric. These high end tails correspond to narrow regions of strong stretching that can be important in the mixing of passive scalars.

In Fig. 9, we compare the rescaled log stretching fields themselves for different N, for the random array flow. Both the high and low Re cases are shown. It may be seen that the rescaled log stretching fields are not strongly dependent on N. However, there is some visible difference between $N = 2,3$ for the high Re case.

We quantify the similarity between the rescaled stretching fields by computing the cross correlation coefficients between the scaled $\log S(x, y)$ fields for various N with those for $N - 1$. As we show in Fig. 10, the fields become more correlated for all of the flows as N increases, indicating that the normalized stretching distributions are converging. This result

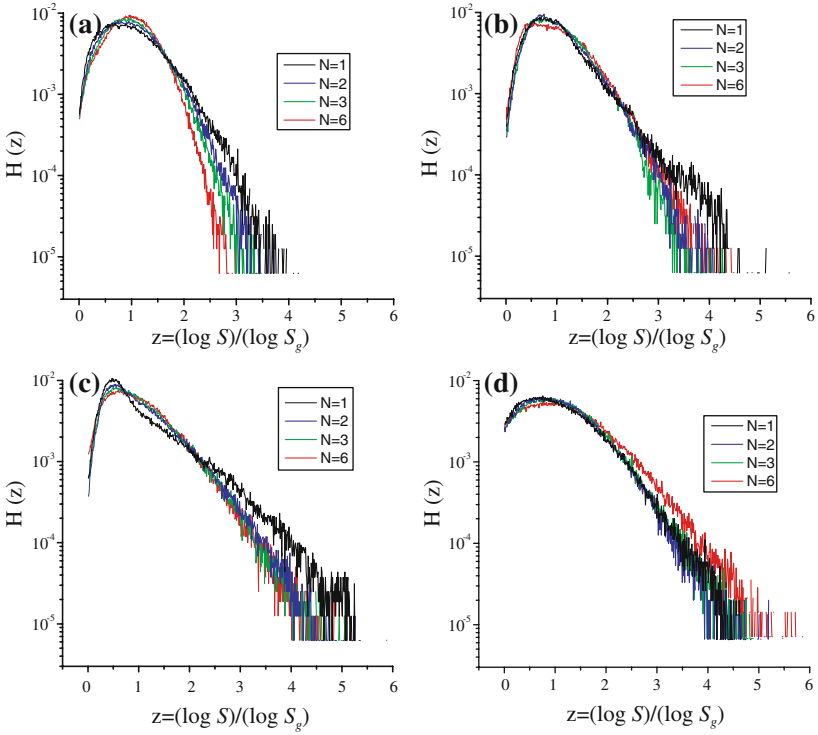

Fig. 8. (Color online) Probability density function of the rescaled logarithm of future stretching $H(z)$, where $z = (\log S)/\log S_g$) for the various flows of Figs. 2 and 3: $N = 1$ (black), 2 (blue), 3 (green), and 6 (red). There is a substantial degree of collapse of the distributions.

can also be observed visually in Fig. 9, where the normalized stretching fields appear to be quite similar, especially at large N.

The geometric mean stretching is expected to grow exponentially with the number N of cycles as $S_g = Ae^{\langle\lambda\rangle N}$, where A is an exponential pre-factor. This hypothesis is tested in Fig. 11, and seems to be consistent with the data, though the evidence is strongest for the high Re random array case.

The scaled distributions for the various flows considered in this paper are compared in Fig. 12. They are quite similar; all of the $\log S$ distributions have a peak, followed by a roughly linear tail in $\log S$. Equivalently, the probability $P(S)$ is approximately a power law function of S for large S.

We compare these experimental results with the existing numerical studies in the following section.

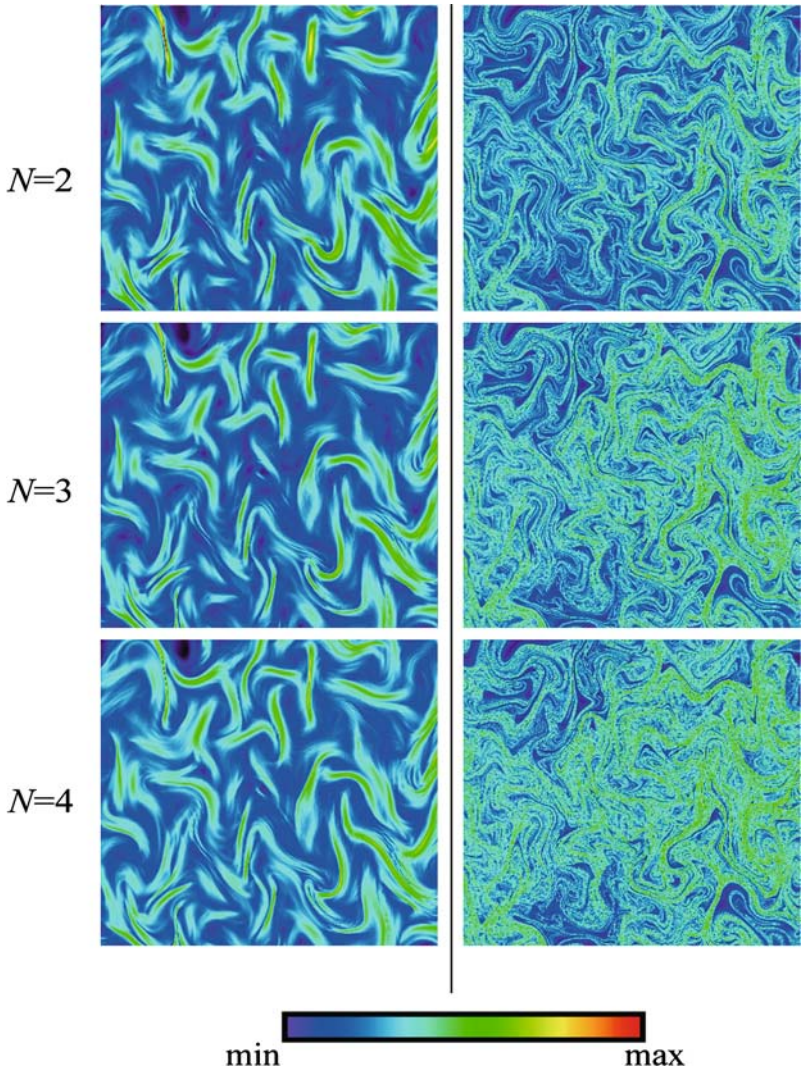

Fig. 9. (Color online) Logarithmic stretching fields, scaled by the logarithm of the geometrical mean stretching, for various numbers N of cycles. Left row: random array, for $Re = 4.5$ and $p = 1.0$. Right row: same flow under more strongly chaotic conditions ($Re = 65$, $p = 2.5$). The normalized fields are not strongly dependent on N.

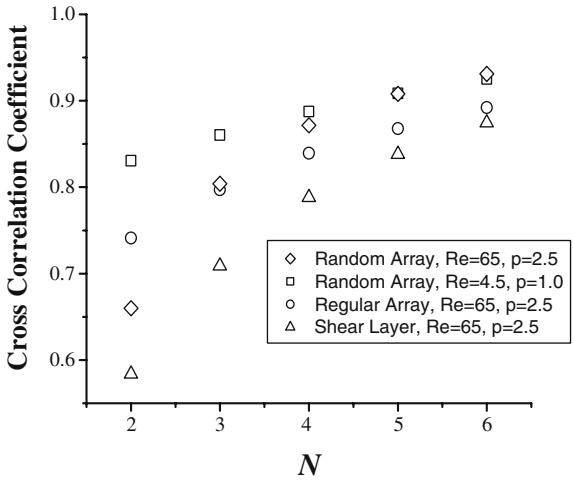

Fig. 10. Cross-correlation coefficient comparing normalized stretching fields for N periods with those for $N = 1$, for the various flows. The correlation grows with N in all cases.

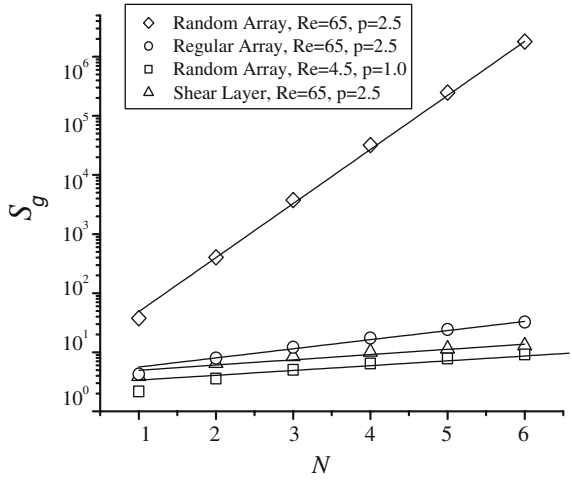

Fig. 11. Geometric mean stretching measured over N periods, for various flows. Exponential behavior is consistent with the data.

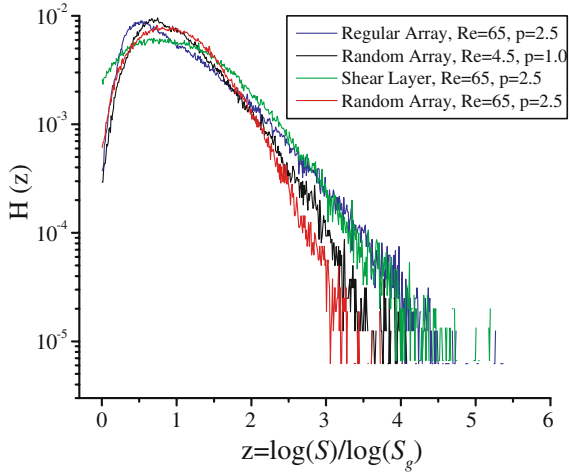

Fig. 12. Comparison of the scaled distributions of ($\log S$) for $N = 3$, for the various flows studied in this paper. The distributions are quite similar to each other.

4. DISCUSSION AND CONCLUSION

In this paper, we discuss the statistics of experimentally measured stretching fields in four different time periodic fluid flows as shown in Figs. 2–5. We selected these flows to explore the role of spatial symmetry, temporal reversibility, and flow dynamics on the behavior of stretching distributions. We experimentally test the hypothesis, previously studied numerically, that stretching fields measured over various numbers of periods should have the same geometrical structure, and should be identical when suitably rescaled. We find these expectations to be generally borne out for the experiments reported here, as indicated in Figs. 6, 8, and 9.

The distributions of $\log S$ (Figs. 7 or 8) show that the stretching is always highly inhomogeneous, and that there are significant regions of low stretching for some flows even over six periods, as shown in Fig. 7(b–d). These are flows with high spatial and temporal symmetry where significant non-chaotic regions are present. For such flows, we find that the distributions of $\log S$ are strongly non-Gaussian. This is in accordance with previous work on 2D incompressible chaotic flows.[10,11] We find that visible non-Gaussian behavior occurs even for flows where regular islands are relatively small (about 7% of the domain), as in Fig. 7(a). Our high *Re* random array flow comes closer to showing a Gaussian stretching distribution, though it is still asymmetric even at $N = 6$. This remaining

asymmetry may be contrasted with some numerical investigations of 2D globally chaotic flows, where the distribution of log S was found to be nearly Gaussian at large N.[5,6]

In this investigation, we rescale the log stretching values by the logarithm of the geometrical mean stretching, which grows linearly in time. As explained in ref. 5, the self-similar behavior of the probability distribution $H(\log S)$ is expected to emerge when stretching is scaled in this way. This seems to be the case approximately (but not perfectly) for all of the flows we investigated experimentally, as shown in Fig. 8. In general, for all flows, the rescaled stretching distribution is not lognormal. The distributions show enhanced tails on the high end, rendering them asymmetric.

We find that the data collapse of $H(z)$, where $z = (\log S)/(\log S_g)$, improves with N. This observation is in agreement with previous work[17] on nonlinear mappings, in which $(\log S)/\Delta t$ is observed to converge pointwise at almost all positions as time (or N) increases. This is also an expectation from large deviation theory.[22] Of course, initial anomalies are expected at early times. Note that both scalings are equivalent, $(\log S)/\Delta t$ and $(\log S)/(\log S_g)$, since $(\log S_g)$ is approximately a linear function of N. We also find that the rescaled log stretching fields themselves become very similar at larger N. This similarity is quantified by calculating the cross correlation coefficient of the normalized field at time N with that for $N-1$. As shown in Fig. 10, the rescaled stretching fields for all of the flows are highly correlated at large N.

As we show in Fig. 11, S_g grows exponentially with N for the random array case at $Re = 65$ ($p = 2.5$), with $A = 5.9$ and $\langle\lambda\rangle = 2.1$. The constraint imposed by spatial symmetry on the velocity field and consequently on chaotic motion becomes apparent in the lower value of $\langle\lambda\rangle = 0.35$ for the regular array case at $Re = 65$ ($p = 2.5$). In this flow the spatial lines of reflection symmetry create many regions of non-chaotic flow. A lower growth rate of stretching with N is also observed for the shear layer flow ($Re = 65$, $p = 2.5$, $\langle\lambda\rangle = 0.2$) which also has lines of reflection symmetry, though only along one axis. Next we examine the random array case at a lower speed and path length ($Re = 4.5$, $p = 1.0$). This flow has a smaller measured violation of temporal reversibility than does the same flow at higher Re, and the geometric mean stretching grows at a much smaller rate ($\langle\lambda\rangle = 0.18$). In fact, the slow growth of the geometric mean suggests the existence of large regular regions in the flow.

Note that the particle motion described in this paper is analogous to the phase space behavior of a Hamiltonian dynamical system, and therefore may show both regular and chaotic regions. However, the degree of departure from time-reversibility, which is affected by inertia (i.e., Re), determines the spatial extent of the regular regions. For small Re, there are

large regular regions where particles are locally subjected to linear, instead of exponential, growth of small displacements.

Remarkably, the normalized distributions for the various flows are very similar, despite the fact that the flows have quite different characteristics such as magnet arrangements and values of Re and p. In fact, one may *a priori* expect different distributions for different flows. The similarity of the scaled distributions for different flows remains to be explained. One possible source of asymmetry might be an enhancement of low stretching values due to particles spending more time near regular islands, as discussed by ref. 23. However, our distributions appear to be enhanced on the high side.

ACKNOWLEDGMENTS

We would like to thank George Haller for fruitful discussions. Greg Voth developed the method for measuring stretching fields that is used here. Mike Rivera suggested the magnet configuration for the shear layer flow. This work was supported by National Science Foundation Grant DMR-0405187. JPG appreciates the hospitality of the University of California at Santa Barbara during the preparation of this manuscript.

REFERENCES

1. R. T. Pierrehumbert, Large-scale horizontal mixing in planetary atmospheres, *Phys. Fluids A* **3**:1250–1260 (1991).
2. T. Akira, R. A. Rogers, P. E. Hydon, and J. P. Butler, Chaotic mixing deep in the lung, *Proc. Natl. Acad. Sci*. **99**:10173–10178 (2002).
3. G. K. Batchelor, The effect of homogeneous turbulence on material lines and surfaces, *Proc. R. Soc. London Ser. A* **213**:349–368 (1952).
4. H. Aref, Stirring by chaotic advection, *J. Fluid Mech*. **143**:1–21 (1984).
5. J. M. Ottino, F. J. Muzzio, M. Tjahjadi, J. G. Franjione, S. C. Jana, and H. A. Kusch, Chaos, symmetry, and self-similarity: Exploiting order and disorder in mixing processes, *Science* **257**:754–760 (1992).
6. X. Z. Tang and A. H. Boozer, Finite time Lyapunov exponent and advection–diffusion equation, *Physica D* **95**:283–305 (1996).
7. G. A. Voth, G. Haller, and J. P. Gollub, Experimental measurements of stretching fields in fluid mixing, *Phys. Rev. Lett*. **88**:254501 (2002).
8. J. M. Ottino, *The Kinematics of Mixing: Stretching, Chaos, and Transport*. (Cambridge University Press, 1989).
9. G. A. Voth, T. C. Saint, G. Dobler, and J. P. Gollub, Mixing rates and symmetry breaking in two-dimensional chaotic flow, *Phys. Fluids* **15**:2560–2566 (2003).
10. E. Ott and T. M. Antonsen, Fractal measures of passively convected vector fields and scalar gradients in chaotic fluid flows, *Phys. Rev. A* **39**:3660–3671 (1989).
11. F. Varosi, T. M. Antonsen, and E. Ott, The spectrum of fractal dimensions of passively convected scalar gradients in chaotic fluid flows, *Phys. Fluids A* **3**:1017–1028 (1991).

12. F. J. Muzzio, P. D. Swanson, and J. M. Ottino, The statistics of stretching and stirring in chaotic flows, *Phys. Fluids* **3**:822–834 (1991).
13. M. A. Sepulveda, R. Badii, and E. Pollak, Spectral analysis of conservative dynamical systems, *Phys. Rev. Lett*. **63**:1226–1229 (1989).
14. R. T. Pierrehumbert, Decay of passive scalars under the action of single scale smooth velocity fields in bounded two-dimensional domains: From non-self-similar probability distribution functions to self-similar eigenmodes, *Phys. Rev. E*. **66**:056302 (2002).
15. E. R. Abraham and M. M. Bowen, Chaotic stirring by a mesoscale surface ocean-flow, *Chaos* **12**:373–381 (2002).
16. A. Prasad and R. Ramaswamy, Characteristic distributions of finite-time Lyapunov exponents, *Phys. Rev. E*. **60**:2761–2766 (1999).
17. V. I. Oseledec, A multiplicative ergodic theorem. Lyapunov characteristic numbers for dynamical systems, *Trans. Moscow. Math. Soc*. **19**:197–231 (1968).
18. A. Androver and M. Giona, Long-range correlation properties of area-preserving chaotic systems, *Physica A* **253**:143–153 (1998).
19. D. Beigie, A. Leonard, and S. Wiggins, A global study of enhanced stretching and diffusion in chaotic tangles, *Phys. Fluids A* **3**:1039–1050 (1991).
20. F. J. Muzzio, C. Meneveau, P. D. Swanson, and J. M. Ottino, Scaling and multifractal properties of mixing in chaotic flows, *Phys. Fluids A* **4**:1439–1456 (1992).
21. J. G. Franjione and J. M. Ottino, Symmetry concepts for the geometric analysis of mixing flows, *Phil. Trans. R. Soc. Lond. A* **338**:301–323 (1992).
22. R. S. Ellis, *Entropy, Large Deviations, and Statistical Mechanics* (Springer-Verlag, New York, 1985).
23. T. Horita, H. Hata, and H. Mori, Long-time correlations and expansion-rate spectra of chaos in Hamiltonian systems, *Prog. Theor. Phys*. **83**:1065–1070 (1990).